AGU PUBLICATIONS

JGR

Journal of Geophysical Research: Atmospheres

RESEARCH ARTICLE
10.1002/2015JD023786

Key Points:
- The first no-gap OH airglow all-sky imager network in the world
- Large number of CGWs were observed by the network in August 2013
- Multialtitude observations for the CGWs by groundbased network and satellites

Supporting Information:
- Text S1 and Captions for Movies S1 and S2
- Movie S1
- Movie S2

Correspondence to:
J. Xu,
xujy@nssc.ac.cn

Citation:
Xu, J., et al. (2015), Concentric gravity waves over northern China observed by an airglow imager network and satellites, *J. Geophys. Res. Atmos.*, *120*, 11,058–11,078, doi:10.1002/2015JD023786.

Received 11 JUN 2015
Accepted 8 OCT 2015
Accepted article online 11 OCT 2015
Published online 3 NOV 2015

Concentric gravity waves over northern China observed by an airglow imager network and satellites

Jiyao Xu[1], Qinzeng Li[1], Jia Yue[2], Lars Hoffmann[3], William C. Straka III[4], Cuimei Wang[1], Mohan Liu[1], Wei Yuan[1], Sai Han[5], Steven D. Miller[6], Longchang Sun[1], Xiao Liu[1,7], Weijun Liu[1], Jing Yang[8], and Baiqi Ning[9]

[1]State Key Laboratory of Space Weather, Center for Space Science and Applied Research, Chinese Academy of Sciences, Beijing, China, [2]Atmospheric and Planetary Sciences, Hampton University, Hampton, Virginia, USA, [3]Jülich Supercomputing Centre, Forschungszentrum Jülich, Jülich, Germany, [4]Cooperative Institute for Meteorological Satellite Studies, University of Wisconsin-Madison, Madison, Wisconsin, USA, [5]Dalian Meteorological Observatory, Dalian, China, [6]Cooperative Institute for Research in the Atmosphere, Colorado State University, Fort Collins, Colorado, USA, [7]College of Mathematics and Information Science, Henan Normal University, Xinxiang, China, [8]Institute of Atmospheric Physics, Chinese Academy of Sciences, Beijing, China, [9]Institute of Geology and Geophysics, Chinese Academy of Sciences, Beijing, China

Abstract The first no-gap OH airglow all-sky imager network was established in northern China in February 2012. The network is composed of six all-sky airglow imagers that make observations of OH airglow gravity waves and cover an area of about 2000 km east and west and about 1400 km south and north. An unusual outbreak of Concentric Gravity Wave (CGW) events were observed by the network nearly every night during the first half of August 2013. These events were coincidentally observed by satellite sensors from Fengyun-2 (FY-2), Atmospheric Infrared Sounder (AIRS)/Aqua, and Visible Infrared Imaging Radiometer Suite (VIIRS)/Suomi National Polar-orbiting Partnership (NPP). Combination of the ground imager network with satellites provides multilevel observations of the CGWs from the stratosphere to the mesopause region. In this paper, two representative CGW events in August 2013 are studied in detail: first is the CGW on the night of 13 August 2013, likely launched by a single thunderstorm. The temporal and spatial analyses indicate that the CGW horizontal wavelengths follow freely propagating waves based on a GW dispersion relation within 300 km from the storm center. In contrast, the more distant observed gravity wave field exhibits a smaller horizontal wavelength of ~20 km, and our analysis strongly suggest this wave field represents a ducted wave. A second event, exhibiting multiple CGWs, was induced by two very strong thunderstorms on 9 August 2013. Multiscale waves with horizontal wavelengths ranging from less than 10 km to 200 km were observed.

1. Introduction

It is well known that gravity waves play an important role in controlling the dynamics and thermal balance in the mesosphere and lower thermosphere (MLT) region [e.g., *Fritts and Alexander*, 2003]. In particular, convectively generated concentric gravity waves (CGWs) and their impact on the middle and upper atmosphere have been studied by several investigators using numerical simulations [e.g., *Piani et al.*, 2000; *Lane et al.*, 2003; *Horinouchi et al.*, 2002; *Alexander et al.*, 2004; *Vadas et al.*, 2009, 2012].

CGWs have been observed using single airglow imagers for decades [e.g., *Taylor and Hapgood*, 1988; *Sentman et al.*, 2003; *Suzuki et al.*, 2007a; *Yue et al.*, 2009, 2013; *Vadas et al.*, 2009, 2012]. *Taylor and Hapgood* [1988] first reported a CGW event in the O_2, Na, OH airglow emissions and found a thunderstorm near the center of the concentric wave. *Sentman et al.* [2003] simultaneously observed CGWs and sprites, both of which were associated with a severe thunderstorm in the U.S. Great Plains. *Suzuki et al.* [2007a] suggested that a weak wind system in the middle atmosphere is a favorable condition for CGW propagation. *Yue et al.* [2009] reported nine CGWs from 2003 to 2008 using an OH airglow imager at the Yucca Ridge Field Station near Fort Collins, Colorado. They found that deep convective plumes occurred near all of the CGW centers. Moreover, *Yue et al.* [2013] first reported simultaneous observations of CGWs in the mesosphere from a ground-based OH airglow imager and the stratosphere from the Atmospheric Infrared Sounder (AIRS) onboard the Aqua satellite. *Suzuki et al.* [2013a], using a chain of three OH airglow imagers in Japan, first presented a larger-scale CGW that originated from a typhoon.

Compared with a single airglow imager, an all-sky airglow imager network can cover a wider spatial range and provide an excellent platform to investigate both large-scale and small-scale GWs while maintaining detailed insight into the GW temporal and spatial evolution. Most notably, the generation of CGWs is often associated with strong thunderstorms, which can often block a single all-sky airglow imager's field of view. The all-sky airglow imager network can remedy this limitation.

The first no-gap all-sky OH airglow imager network in the world was built in northern China in 2012. CGWs were observed by the imager network almost every night in the first half of August 2013. Such a high occurrence frequency of CGWs from any ground observations is rare. *Yue et al.* [2009] reported only nine CGW events out of 8 years of observations. Furthermore, in this paper, we discuss the first simultaneous observations of CGW propagations from the cloud map near the tropopause by the Fengyun-2 (FY-2) satellite, in the stratosphere by AIRS/Aqua, and in the mesopause region by the ground-based all-sky airglow imagers network and Visible Infrared Imaging Radiometer Suite (VIIRS)/Suomi National Polar-orbiting Partnership (NPP).

This paper is arranged as follows: section 2 gives information about the no-gap all-sky OH imager network and satellite observations. The CGW events observed by the network and the satellites in August 2013 are presented in section 3. Two case studies are presented. Section 3 also compares network observations from 2012 to 2014. The summary is given in section 4.

2. Observations

2.1. No-Gap OH All-Sky Airglow Imager Network

We established a network of OH airglow all-sky imagers in northern China, which began data acquisition in February 2012. Every OH airglow imager is composed of a 1024×1024 pixel CCD detector ($13 \times 13\ \mu m^2$ pixel size, imaging area is $13.3 \times 13.3\ mm^2$), a near-infrared (NIR) band (715–930 nm) filter with a notch centered at 865.5 nm to suppress the O_2 (0, 1) emission, a Nikon 16 mm/2.8D fisheye lens with a field of view of 180°, and an optical imaging system. The exposure time is 1 min. The spatial resolution of the airglow imager at the OH layer is not uniform; it is about 0.27 km at zenith, 0.52 km at the zenith angle of 45°, and about 5.5 km at the zenith angle of 80°. The network is composed of 6 airglow imagers (Figure 1). Three imager stations are located near 40°N: Shuozhou (39.8°N, 112.1°E), Xinglong (40.4°N, 117.6°E), and Donggang (40.0°N, 124.0°E). The other three stations are near 36°N: Xinxiang (35.7°N, 113.7°E), Linqu (36.2°N, 118.7°E), and Rongcheng (37.3°N, 122.5°E). Among these stations, the earliest observation began at the Xinglong station in November 2009 during the Meridian Space Weather Monitoring Project [*Wang,* 2010; *Li et al.*, 2011]. The latest began in February 2012 at the Donggang station (40.0°N, 124.0°E). The distances between two neighboring stations vary from 450 km to 550 km. Table 1 gives the dates on which observation began and details about the locations of the all-sky airglow imagers in northern China. Every all-sky imager has the field of view of 180°. However, for some stations, the edge of airglow image is contaminated by ambient light and ground objects (such as houses and trees). On the other hand, with the increase of zenith angle, the airglow image is strongly distorted due to the fisheye effect. Therefore, we assume the effective field of view of every instrument used being 160° (i.e., gravity waves can be clearly viewed with the zenith angle smaller than 80° without being obstructed). Every all-sky imager can make gravity wave observations with a radius of 420 km at ~87 km altitude. Figure 1 shows the positions of the all-sky airglow imager stations and their horizontal coverage. This network configuration can make observations over an area of ~2000 km east-west and 1400 km north-south.

The raw OH airglow images are processed as follows. First, the images are calibrated using the method described by *Garcia et al.* [1997]. Second, we remove the van Rhijin effect and atmospheric extinction according to *Kubota et al.* [2001]. The observed airglow images are affected by the van Rhijin effect. The airglow emission intensity at zenith angle θ can express as

$$I(\theta) = I(0) \cdot V(H, \theta),$$
$$V(H, \theta) = \left[1 - \left(\frac{R}{R+H}\right)^2 \sin^2(\theta)\right]^{-1/2}, \quad (1)$$

where $I(0)$ is the emission intensity at zenith. $V(H, \theta)$ is the van Rhijn correction factor. R is the earth radius and H is the height of OH airglow layer. The observed airglow images are also affected by atmospheric extinction.

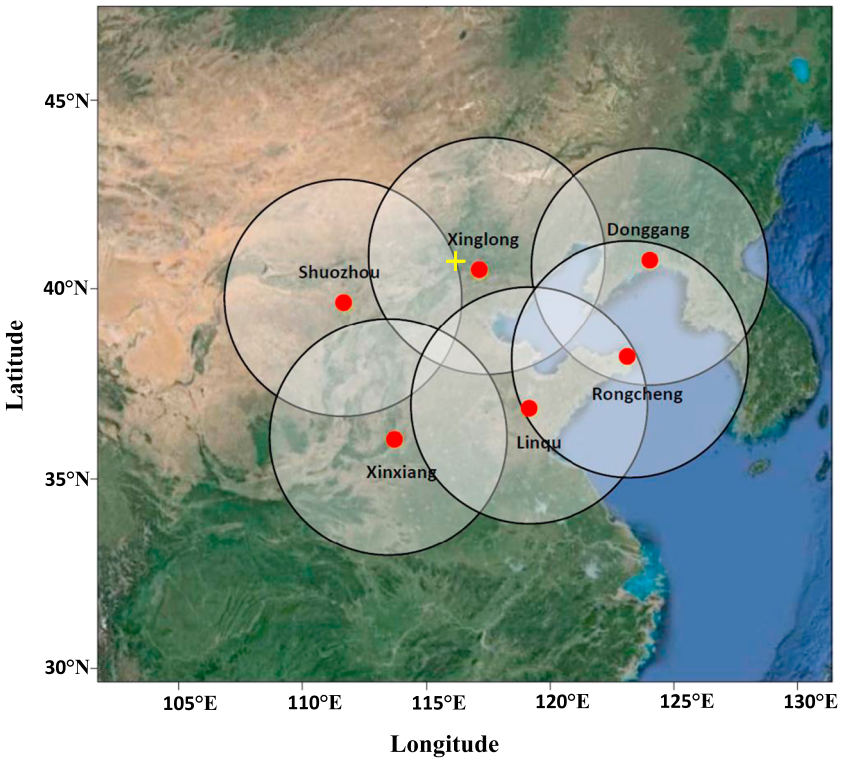

Figure 1. The network of the all-sky airglow observations in northern China. The radius of the circle is 420 km, which corresponds to a zenith angle of 80° at a height of 87 km. The yellow cross indicates the location of the meteor radar.

The relation between observed emission intensity $I(\theta)$ at ground and true emission intensity $I_{true}(\theta)$ at airglow emission layer is addressed by *Kubota et al.* [2001]:

$$I(\theta) = I_{true}(\theta)\cdot 10^{-0.4\cdot\alpha\cdot F(\theta)},$$
$$F(\theta) = \left[\cos\theta + 0.15\cdot\left(93.885 - \theta\cdot\frac{180}{\pi}\right)^{-1.253}\right]^{-1}, \quad (2)$$

where α is the atmospheric extinction coefficient and $F(\theta)$ is an empirical equation.

Therefore, combining equations (1) and (2), the image correction factor can be written as

$$K = V(H,\theta)\cdot 10^{-0.4\cdot a\cdot F(\theta)}. \quad (3)$$

The parameter α is related to the atmospheric observation environment. Here we assume the parameter α is constant during the time of the CGW event observed in the image. The averaged image can be obtained during the time. From the averaged image, we can get the airglow intensity profile with the change of zenith angle. By comparing the intensity profile from the observed airglow image and K profiles under different values of α, the value of α is used from when the two profiles fit best. The raw images are divided by the correction factor K to achieve flat field of the airglow image. In order to enhance wave features, time-difference (TD) images are obtained by subtracting two consecutive images. Then the time-difference images are projected onto the geographical coordinates with a size of 840 km × 840 km grid assuming the altitude of the OH airglow layer at 87 km [*Li et al.*, 2011, 2013].

Table 1. The Locations of All-Sky Airglow Imagers

Station	Location	Begin of Observation
Shuozhou	(39.8°N, 112.1°E)	Jan 2012
Xinglong	(40.4°N, 117.6°E)	Nov 2009
Donggang	(40.0°N, 124.0°E)	Feb 2012
Xinxiang	(35.7°N, 113.7°E)	Jan 2012
Linqu	(36.2°N, 118.7°E)	Dec 2011
Rongcheng	(37.3°N, 122.5°E)	Jan 2012

The horizontal wavelength at a specific location in the direction of the wave vector is calculated from two consecutive wave crests. The moving distance of the two wave crests between the time

Table 2. Satellite Observations Used in This Work

Instrument	Measurement	Purposes
Suomi NPP/VIIRS	Infrared and visible radiation (DNB); infrared 11 μm band.	Gravity waves in the mesopause region; cloud image in the troposphere
Aqua/AIRS	Atmospheric temperature (4.3 μm and 8.1 μm)	Gravity waves in the stratosphere and cloud image in the troposphere
FY-2D and FY-2E	Cloud images in China area in infrared band (10.3–11.3 μm).	Temporal variation of the cloud distribution

interval of two images can be measured, respectively. The average moving distance of two wave crests is used as the displacement of the crest. Then, the observed speed is estimated from the displacement of the crest between the time interval of two images. The time interval between two consecutive images is 1 min.

2.2. VIIRS, AIRS, and Fengyun-2 Satellite Observations

The Suomi NPP satellite operates in a Sun-synchronous orbit at 824 km above the Earth. The VIIRS sensor is one of the five payloads, employing a multispectral scanning imager that can capture high-resolution visible and infrared images. The Day Night Band (DNB) channel on the VIIRS is a visible/near-infrared (NIR) sensor with a spectral range from 500 to 900 nm, which coincides with part of the OH Meinel (NIR) band (382–4470 nm) [*Chamberlain*, 1961] and the OI band (577 nm) [*Miller et al.*, 2012]. The contribution of OI emission is smaller in comparison to the OH. Therefore, we ignore the OI emission contribution. The high spatial resolution of the VIIRS is 0.375 km at the nadir view for imagery resolution bands and 0.75 km for moderate resolution bands. The across-track swath width of the VIIRS is 3000 km [*Yue et al.,* 2014]. In this work, VIIRS/DNB combined with ground-based OH airglow imagers provides an excellent opportunity to study the mesospheric gravity waves. The infrared band (11 μm) of VIIRS gives cloud brightness temperature (which is a measurement of the radiance of the cloud, expressed in units of the temperature of an equivalent black body) of convective clouds as the stratosphere is transparent at this wavelength.

AIRS is one of the six instruments onboard the Aqua satellite launched in May 2002. The satellite flies in a Sun-synchronous orbit at an altitude of 705 km [*Aumann et al.*, 2003]. Stratospheric gravity waves are observed by AIRS radiance measurements at 4.3 μm and 15 μm [*Hoffmann and Alexander*, 2010; *Hoffmann et al.*, 2013; *Gong et al.*, 2012; *Gong et al.*, 2015]. The swath width of AIRS is 1765 km. The footprint size is 13.5 km × 13.5 km at the nadir view and 41 km × 21.4 km at the scan edges [*Yue et al.*, 2014]. In this study, we focus on the 4.3 μm measurements of temperature perturbations at an altitude range of 30–40 km. Deep convective clouds can be detected by the AIRS radiance measurements at 8.1 μm [*Aumann et al.*, 2006; *Hoffmann and Alexander*, 2010].

Fengyun-2 (FY-2) is the first-generation Chinese geostationary meteorological satellites series (http://www.nsmc.cma.gov.cn/en/NSMC/Home/index.html). Fengyun-2D (FY-2D) and Fengyun-2E (FY-2E) belong to the

Table 3. The Cluster Events of CGWs Observed from Network All-Sky Airglow Imagers and Satellite Observations in August 2013[a]

Day (In Aug 2013)	Duration (Local Time)	Position of CGWs Center	All-Sky Airglow Imagers	AIRS	VIIRS/DNB
#3-4	20:50–02:50	(37.3 ± 0.1°N, 108.0 ± 0.2°E)	6	√	
#4-5	20:50–03:58	Multicenters	4	√	
#5-6	22:30–03:58	(35.8 ± 0.2°N, 117.1 ± 0.2°E)	4	√	
#6-7	00:00–04:08	X	2	√	
#8-9	00:07–04:08	(39.8 ± 0.4°N, 113.1 ± 0.3°E)	4	√	√
#9-10@1	20:30–04:08	(35.1 ± 0.6°N, 116.6 ± 0.3°E)	5	√	√
#9-10@2		(34.5 ± 0.1°N, 116.4 ± 0.1°E)			
#10-11	20:57–03:47	Multicenters	5	√	
#12-13	21:30–23:30	(36.2 ± 0.1°N, 115.3 ± 0.1°E)	5	√	√
#13-14	21:30–04:08	(38.6 ± 0.1°N, 114.8 ± 0.2°E)	5		√
#14-15	23:12–03:28	(38.7 ± 0.1°N, 114.7 ± 0.1°E)	4	√	√
#15-16	00:42–03:58	(39.6 ± 0.2°N, 114.7 ± 0.2°E)	3		√
#16-17	20:50–03:57	(38.3 ± 0.1°N, 114.1 ± 0.1°E)	2	√	
#17-18	01:10–03:58	X	3		

[a]Check sign indicates CGWs are observed from satellite observations. Cross means cannot identify the position of CGW center. Plus-minus sign indicates the standard deviation. Multicenters mean several CGWs are observed.

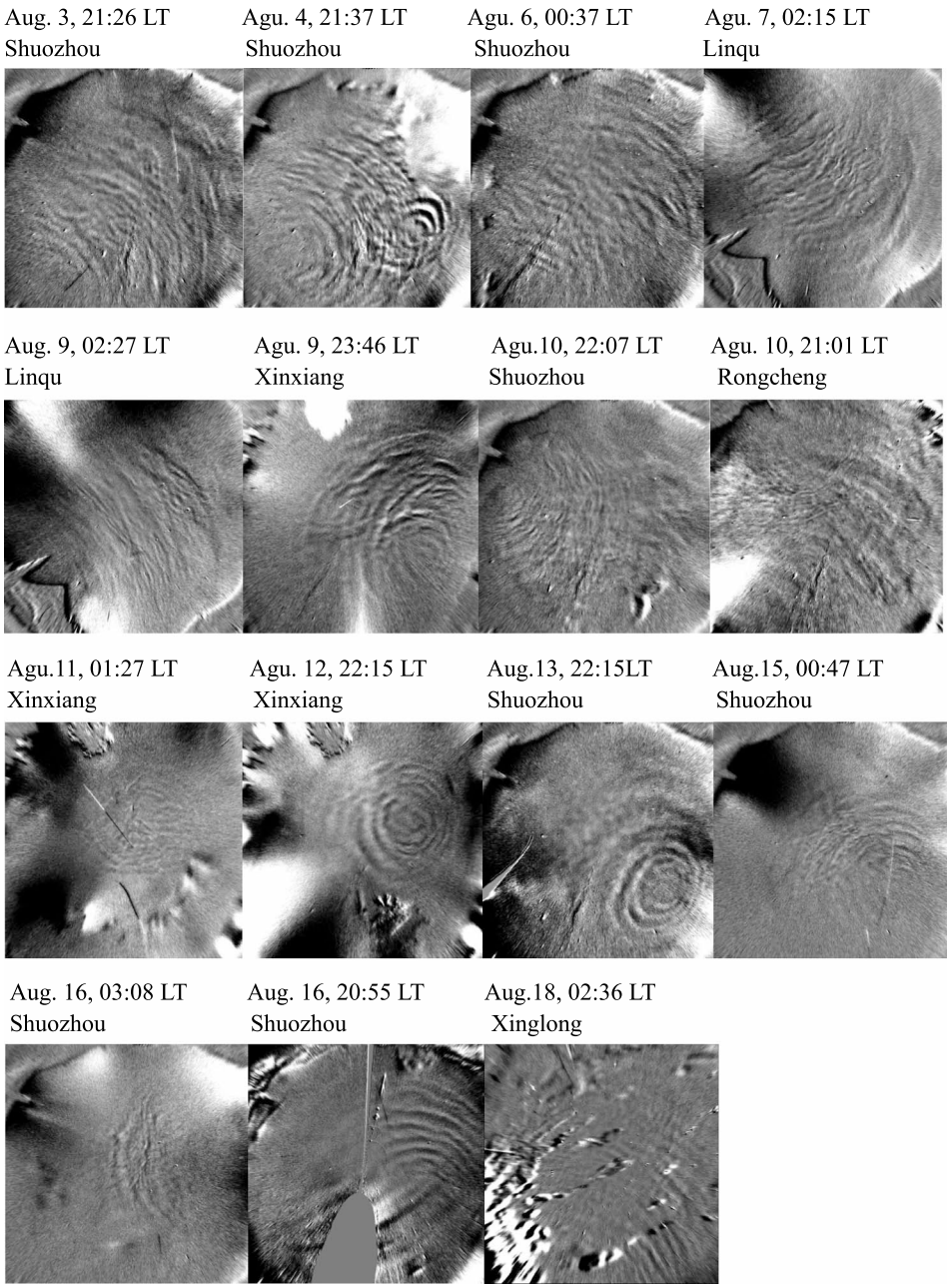

Figure 2. CGWs from unwarped TD OH airglow image observed in 13 nights in August 2013. The images correspond to an area of 800 km × 800 km.

FY-2 satellites series. FY-2D and FY-2E are positioned at 86.5°E and 105°E, respectively. The multichannel scanning radiometers on board FY-2D and FY-2E can provide continuous water vapor and cloud images over China in the visible and infrared bands. In this study, the infrared channel with wavelengths of 10.3 ~ 11.3 μm is used. The Dalian Meteorological Observatory provides the infrared images under the Lambert conic projection from FY-2D in a half-hour interval and from FY-2E in an hourly interval. The spatial resolution is 5 km at subsatellite point. To identify the infrared images of FY-2D and FY-2E, the Meteorological Information Comprehensive Analysis and Process System (MICAPS) is utilized. The clouds observed by FY-2D and FY-2E are used to track the temporal evolution of CGW convective sources.

Detailed information on the satellite instruments used in this work is presented in Table 2.

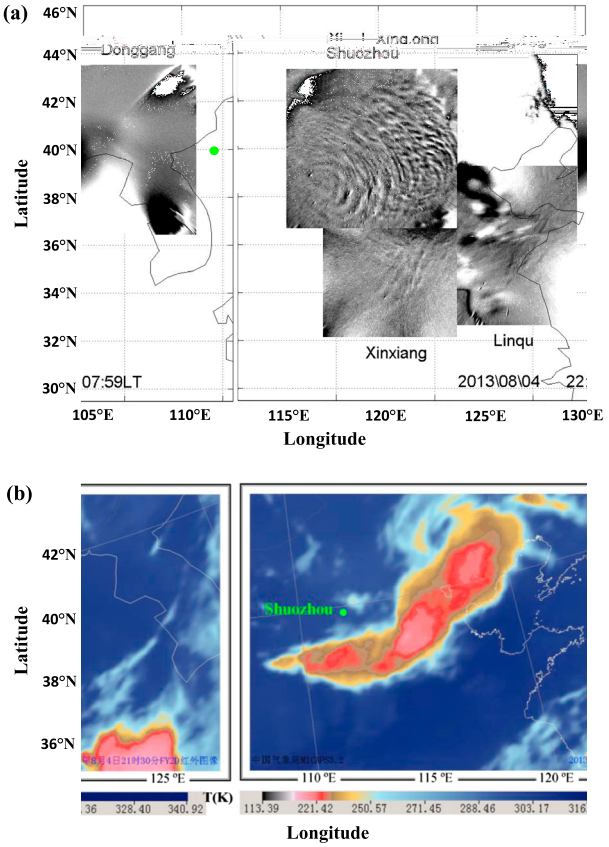

Figure 3. (a) All-sky airglow imager network observation at 22:07 LT on 4 August 2013; (b) FY-2 observations of cloud top brightness temperature under Lambert conic projection at 21:30 LT on 4 August 2013. The green dot is the position of the Shuozhou station.

3. CGW Events in August 2013

The OH airglow imager network in northern China has been in operation since February 2012; of particular interest are 13 nights during the first half of August 2013, where an unusual outburst of CGW was observed by the network. Several of these events were also observed simultaneously by AIRS/Aqua and VIIRS/Suomi NPP.

Table 3 lists these CGW events in August 2013 observed by the OH airglow imager network and satellites. Figure 2 displays the CGW events observed by all-sky airglow image network over northern China on the 13 nights of August 2013. The shapes of CGWs vary from one night to another. On some nights, we can estimate the centers of the CGWs, such as days 3, 5, 8, 9, 12, 13, 14, 15, and 16 in August. Also, multiple CGWs simultaneously showed up on the nights of 4 and 9 August. We consider the CGW event on the night of 4 August 2013 (#4-5) to illustrate the strength of the distributed airglow imager array and simultaneous satellite measurements to determine the gravity source origin. More than two CGW events were simultaneously observed by the all-sky airglow imager at the Shuozhou station (Figure 3a). One CGW in the southwest of the Shuozhou station and a chain of CGWs in the southeast were simultaneously observed at 22:07 LT (Figure 3a). Figure 3b gives the FY-2 observations of high clouds at 21:30 LT. A single storm was located southwest of the Shuozhou station, and a storm cluster was located in the southeast. Therefore, the multiple CGW events in the OH airglow layer were most likely excited by both the single storm and the cluster storms.

Airglow CGWs are usually elliptical because the background wind distorts the gravity waves [*Vadas et al.*, 2009]. In order to locate the CGW center accurately, we fit concentric rings with an elliptic equation by a least squares method. Figure 4 gives an example of the airglow image observed at 22:00 LT on the night of 13 August 2013 near the Shuozhou station. The red dot denotes the estimated center of the CGW, which are calculated every 5 min. Then, the averaged positions of each CGW event and the uncertainties are calculated. These are listed in Table 3. Among the CGW events in August 2013, some have multiple storm sources and CGWs appearing at the same time (e.g., #4-5, #9-10, and #10-11). Some CGW centers are difficult to identify precisely because they are near the edge or out of the coverage of the all-sky imager network (e.g., #6-7, #10-11, and #17-18).

Table 3 shows that extensive CGWs (lasting more than 4 h) were captured on 11 nights by the imager network. Due to the weather conditions at some stations (imagers veiled by clouds), each CGW event is not likely observed by all airglow imagers simultaneously. Fortunately, nine nights of CGWs were observed by at least four all-sky airglow imagers, again demonstrating the strength of our distributed array.

The ground all-sky airglow imager network combined with the satellite observations (FY-2, AIRS/Aqua, and VIIRS/Suomi NPP) can provide multilayer measurements with which we can investigate the CGW vertical propagation and evolution. Table 3 shows that 10 nights of CGWs were observed by AIRS and six CGWs were simultaneously observed by the airglow imager network and VIIRS/DNB. Note that the Sun-synchronous nature of Aqua and Suomi NPP can only observe at about 01:30 AM local time. Four nights (#8-9, #9-10, #12-13, and

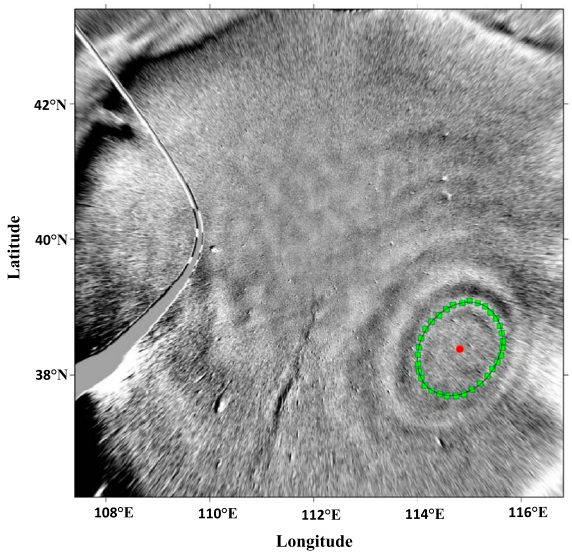

Figure 4. Airglow image was fitted with elliptic equation on the night of 13 August 2013 at 22:00 LT at the Shuozhou station. The green squares represent the brightness of the gravity wave in the airglow. The black line represents the fitting ellipse. The red dot represents the center of the fitting ellipse.

#14-15) of CGWs were simultaneously observed by the all-sky airglow imager network and two satellites (AIRS/Aqua, VIIRS/Suomi NPP). In this study, we present the time evolution of two events in detail, CGW #9-10 and CGW #13-14, in sections 3.2 and 3.3.

3.1. Comparison Between GW Observations in 2012, 2013, and 2014

Thunderstorms are usually produced by strong convective instability and updraft of convective plumes. Convective available potential energy (CAPE) is a good index for convective instability in the troposphere [*Bluestein et al.,* 1988; *Vadas et al.,* 2009]. We use CAPE values from the European Centre for Medium-Range Weather Forecasts (ECMWF) Re-Analysis (ERA-Interim) (http://apps.ecmwf.int/datasets/) [*Dee et al.,* 2011]. The temporal resolution of ERA-Interim

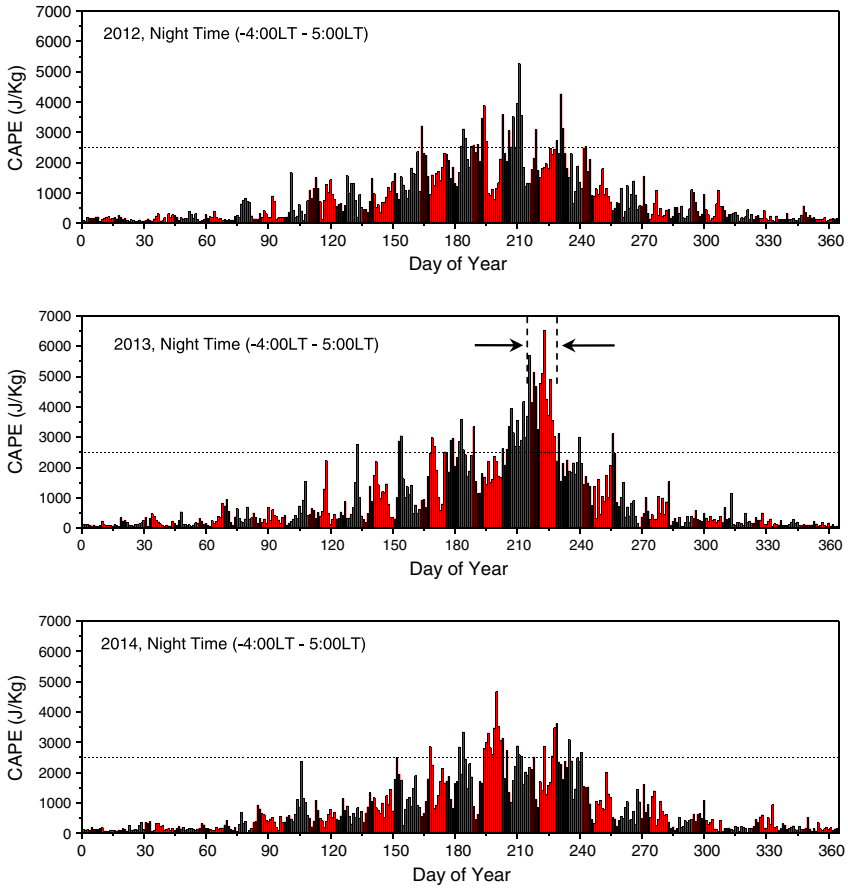

Figure 5. The max value of CAPE in the observation region of the no-gap network in the night (LT: −4:00–5:00; longitude: 32.5°N–45°N; latitude: 105°E–127.5°E) in (top) 2012, (middle) 2013, and (bottom) 2014. The horizontal dashed lines indicate the value of CAPE (2500 (J/kg)). The vertical dashed lines in Figure 5 (middle) indicate the time when the CGW outburst occurred.

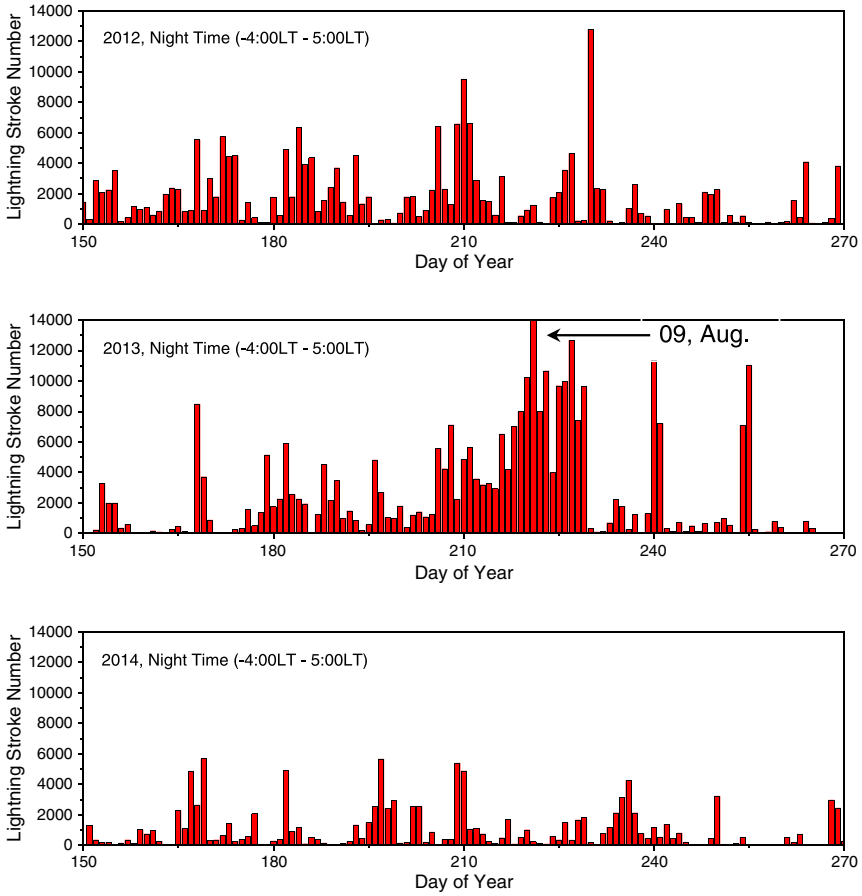

Figure 6. The total lightning stroke count in the observation region of the no-gap network in the night (LT: −4:00–5:00; longitude: 32.5°N–45°N; latitude: 105°E–127.5°E) in (top) 2012, (middle) 2013, and (bottom) 2014.

is 3 h with data at 00, 03, 06, 09, 12, 15, 18, and 21 UTC, and the spatial resolution is 2.5° × 2.5°. We chose the max value of CAPE in the area of the no-gap network at night (LT: −4:00–5:00 or UT: 12:00–21:00; latitude: 32.5°N–45°N; longitude: 105°E–127.5°E) in 2012, 2013, and 2014. The results are shown in Figure 5 and reveal that CAPEs are the largest during the summer and the smallest during the winter. SPC (Storm Prediction Center) of NOAA forecasters refer to CAPE < 1000 J/kg as weak instability, 1000 J/kg < CAPE < 2500 J/kg as moderate instability, 2500 J/kg < CAPE < 4000 J/kg as strong instability, and CAPE > 4000 J/kg as extreme instability [www.spc.noaa.gov/sfctest/help/sfcoa.html]. Due to lack of standardization of the definition of CAPE level, here we use 2500 (J/kg) as the criterion for the strong instability, which may lead to thunderstorms and overshooting. Figure 5 shows that in northern China, strong instability mainly takes place from June to September. Over 3 years the convective unstable days in Summer 2013 is much greater than the other 2 years (21 days in 2012, 39 days in 2013, and 24 days in 2014). It is interesting that during the DOY 205 (24 July) and DOY 229 (17 August) in 2013, CAPEs are more than 2500 (J/kg) continuously.

Another widely used indicator for strong thunderstorms is the lightning flash rate. There is significant support in the literature that lightning activity can be used as a measure of thunderstorm activity [e.g., *Williams et al.,* 2000; *Cummins and Murphy,* 2009]. The observations of lightning of the World Wide Lightning Location Network (WWLLN) [e.g., *Rodger et al.,* 2005, 2006; *Hutchins et al.,* 2012] are used to calculate the lighting stroke count in northern China. Figure 6 gives the total lightning stroke count each night (LT: −4:00–5:00; latitude: 32.5°N–45°N; longitude: 105°E–127.5°E, the same as for the CAPE index) from June to September in 2012, 2013, and 2014. Figure 6 indicates that the total stroke counts in the summer season of 2013 are much larger than those of 2012 and 2014, especially in July and August. During DOY 206 (25 July) to DOY 229 (17 August) in 2013, the total flash counts at night are all larger than 4000. The largest stroke count occurred at DOY 221 (9 August), reaching more than 14,000.

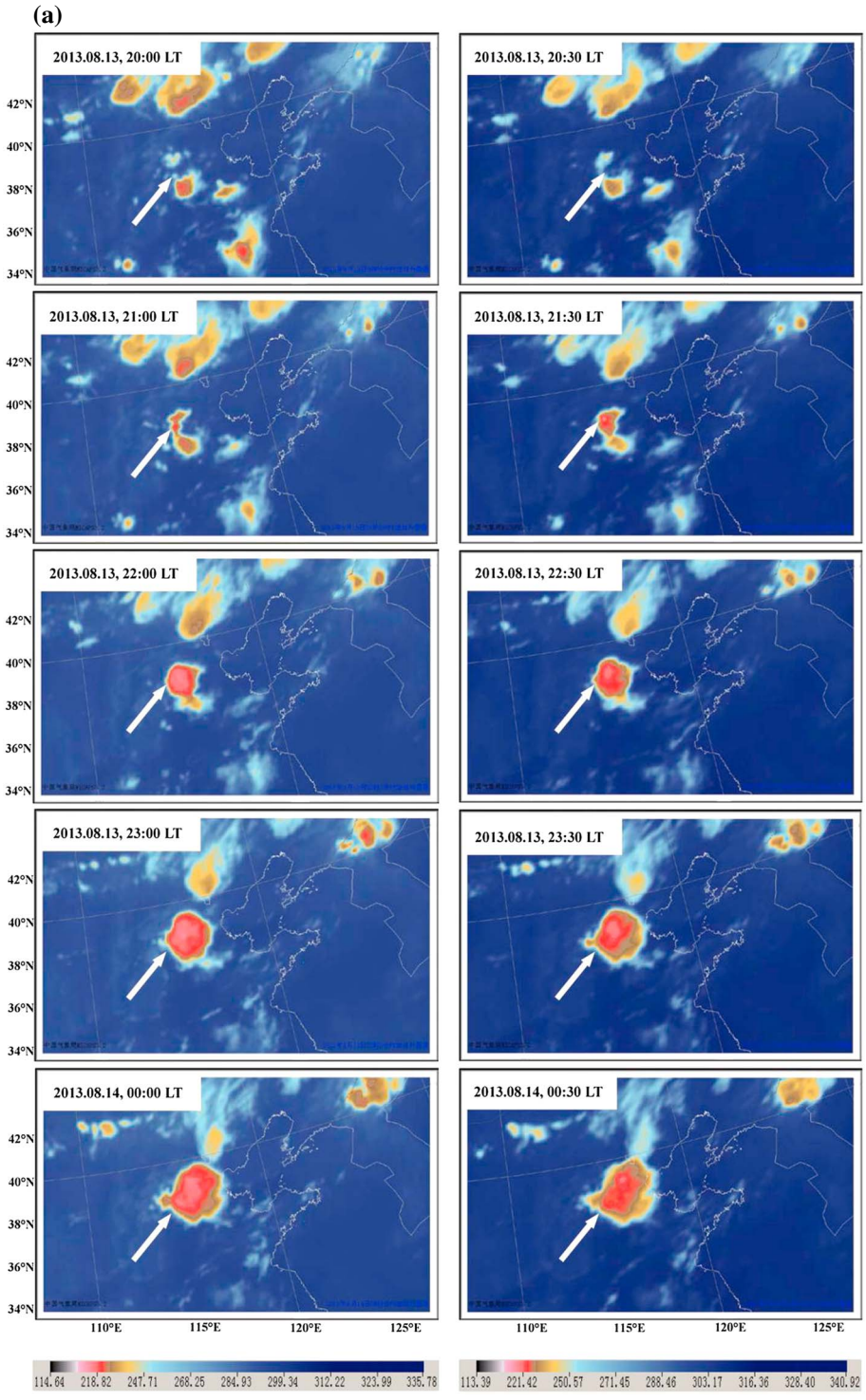

Figure 7. (a) FY-2E (per hour) and FY-2D (per half hour) observations of cloud top brightness temperature from 20:00 LT to 03:00 LT on 13 August 2013; (b) clouds observed by AIRS at 8.1 μm and (c) VIIRS infrared 11 μm on the night of 13 August 2013.

Both the CAPE in Figure 5 and the lightning stroke count in Figure 6 show that unusual frequent and severe thunderstorms took place in the summer season of 2013, especially in the first half August.

The monthly mean of temperature and wind from the reanalysis of the Modern Era Retrospective analysis for Research and Applications (MERRA) [*Rienecker et al.*, 2011] are also investigated (not shown here). There

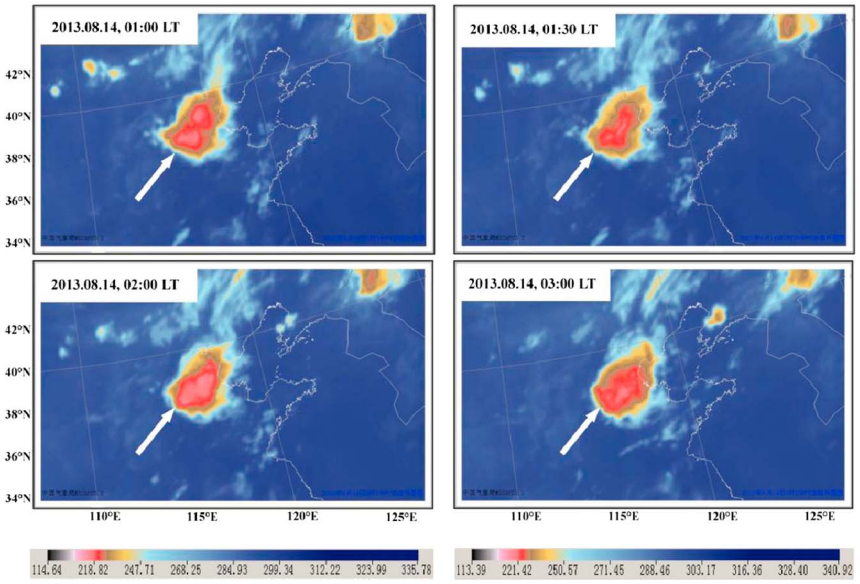

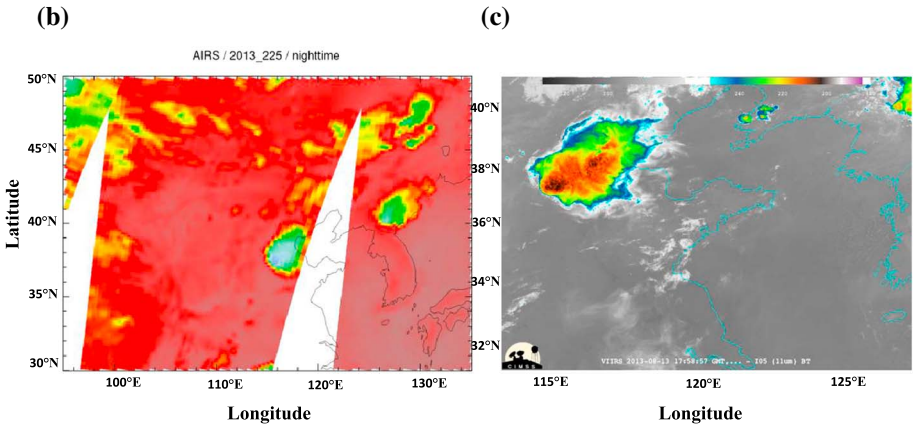

Figure 7. (continued)

were no obvious differences of the atmospheric conditions between the 3 years. This means that the monthly averaged environments of gravity wave propagation are similar for the 3 years. A large number of CGW events were observed in the four summer months (122 days from June to September) in 2012, 2013, and 2014. In 2012, with an exception of the contaminations of moonlight or cloud cover in 42 nights, 18 CGW events in the network were observed. In 2013, 40 CGW events were observed, with an exception of 50 nights that were cloudy or had moonlight contaminations. CGW events were observed by the network almost every night from the DOY 215 (3 August) to DOY 229 (17 August), which corresponds well with the lightning activities shown in Figure 6. However, in 2014 only 15 CGW events were observed. There were 43 cloudy or moonlight-contaminated nights.

The evolutions of two representative CGW events are discussed in detail in following subsections: one is on the night of 13 August, induced by only one strong convective source and another is on the night of 9 August, caused by multiple storm sources.

3.2. Single Source for CGW Event on 13 August (#13-14)

Figure 7a displays the FY-2 cloud imagery from 20:00 LT to 03:00 LT. From Figure 7a we can see that during the night of 13 August 2013 (#13-14), and only one strong convective source of CGW in the region of the all-sky

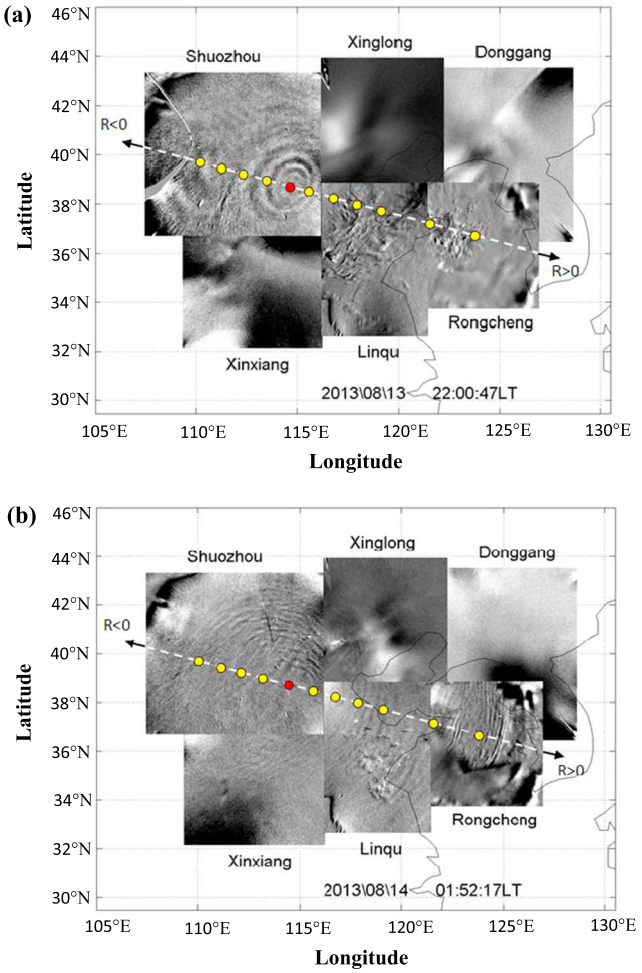

Figure 8. All-sky airglow imager network observation at (a) 22:00 LT and (b) 01:52, respectively. The image along the dashed line crossing the center of the CGW event is used to calculate the wave parameters. The azimuth is east by south 15°. The yellow dots give the positions of radius *R* of −400 km, −300 km, −200 km, −100 km, and 100 km from the Shuozhou station; 200 km, 300 km, and 400 km from the Linqu station; 600 km and 800 km from the Rongcheng station. The red dot indicates the center of the CGW.

imager network lasted longer than 6 h on the FY-2 cloud map, starting from about 21:00 LT to around 03:00 LT. The figure shows the evolution of the thunderstorm as the early maps (20:00 and 20:30 LT) show no obvious activity in the region marked by the white arrows. A thunderstorm located at (38.2°N, 114.9°E) (denoted by the white arrow) began to appear at 21:00 LT. After 21:00 LT, the area of the convective cloud became large and slowly moved eastward. This strong convective cloud was observed in the region of 37.5°N–39.5°N and 114.5°E–117.5°E. After 03:00 LT on 14 August, the observations of the FY-2 show that the cloud top height of this strong convective cloud decreased and the convective cloud gradually disappeared. AIRS observations at 8.1 μm and VIIRS observation at 11 μm shown in Figures 7b and 7c at about 01:30 LT also confirm the location of the storm.

This particular storm generated a strong CGW event that persisted more than 6 h in the OH airglow measurements across the entire network. Movie S1 in the supporting information gives the animated unwarped TD OH airglow images from 20:50 LT to 03:09 LT on 13–14 August 2013 from the all-sky airglow imager network. The CGW event (#13-14) was coincidently observed by five all-sky imagers (Xinglong, Shuozhou, Xinxiang, Linqu, and Rongcheng). It was first observed by Shuozhou station at 21:30 LT until the end of observation in Xinxiang station at 04:08 LT.

The concentric rings seen in the mesopause come from a group of waves that have similar parameters. The size of the ring is determined by the wave parameters. The expansion of the ring over time displayed in the Movie S1 is not due to the horizontal propagation of the wave but rather is due to the later arrival of waves with different parameters (larger horizontal/vertical wavelength ratio) from the thunderstorm [e.g., *Alexander and Holton*, 2004].

Here we study the wave parameters along the line crossing through the center of the CGW event (denoted by the white dashed line in Figure 8) as well as its time evolution. The yellow dots along the white dashed line give the positions of radius *R* of −400 km, −300 km, −200 km, −100 km, and 100 km from Shuozhou station; 200 km, 300 km, and 400 km from Linqu station; and 600 km and 800 km from Rongcheng station. Along the white dashed line, we can get the wave parameters at an extended distance (longer than 1200 km) by combining the Shuozhou, Linqu, and Rongcheng stations. During this event, the other three stations had clouds overhead (see Movie S1).

Figure 9 gives the temporal and spatial horizontal wavelengths variations of the CGW event observed on 13 August 2013. The measured values (dots) as a function of the radius at different local times are marked

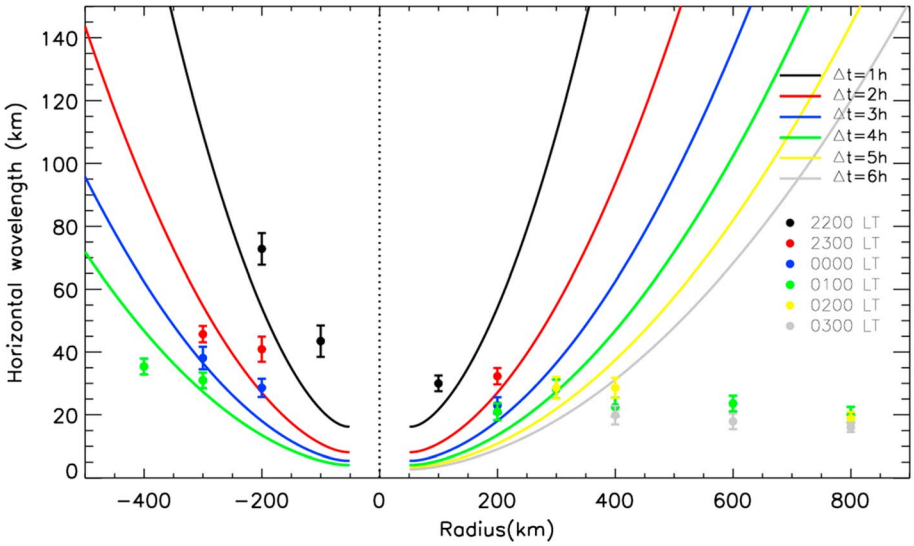

Figure 9. Temporal and spatial horizontal wavelengths variations of CGW event observed on 13 August 2013. The measured values (dots) are derived from the image along the white dashed line in Figure 8. The uncertainties of the horizontal wavelength measurements are calculated 15 min from before and after a fixed observation time. The lines are calculated from GW dispersion relation under the assumption of zero wind. The parameter Δt means the CGW propagation time from the tropopause region to the OH airglow layer.

by different colors in Figure 9**.** The lines are calculated from the GW dispersion relation [*Yue et al.,* 2009] under the assumption of the zero wind,

$$\lambda_h = \frac{2\pi R^2 \left(1 + \Delta z^2 / R^2\right)^{3/2}}{N \Delta z \Delta t}, \tag{4}$$

where λ_h is the horizontal wavelength, Δz is the vertical distance from tropopause to OH airglow layer, and R is the horizontal distance from the constant phase to the observed center of the CGW. N is Brunt-Väisälä frequency. The Δt represents the CGW propagation time from the tropopause region to the OH airglow layer.

The CGW is assumed to be generated at 21:00 LT in the tropopause region because the severe convective cloud started at around 21:00 from the FY-2 cloud imagery (shown in Figure 7a). With the help of the no-gap network, we can derive the wave parameters at a long distance from the wave center. Here we use Shuozhou station data to calculate the parameter of radius R from −400 km to 100 km, Linqu station data from 100 km to 500 km, and Rongcheng station data from longer than 500 km. From Figure 9 we can see that within less than 300 km radius, the measured horizontal wavelengths follow the GW dispersion relationship in the direction of $R < 0$. The figure indicates that there exist some differences between the observation and the GW dispersion relationship. This is because the zero wind assumption in equation (4) is not realistic. However, it is interesting that the horizontal wavelengths for $R > 400$ km are around 20 km with no significant variations in the southeast direction.

The CGW event observed on 13 August 2013 can be seen clearly in the northwest direction but appear weak in the southeast direction (see Movie S1). And longer horizontal wavelength waves are not seen at larger radius. This is probably due to the vertical cancelation. The upward propagating gravity waves with longer vertical wavelengths through the airglow layer can be easily detected from the ground, because of smaller cancelation effect inside the emission layer [*Liu and Swenson*, 2003]. This effect is more significant for larger rings that usually correspond to smaller vertical wavelength waves.

This CGW event was also observed by AIRS/Aqua and VIIRS/Suomi NPP. Figure 10 shows the multilayer multi-instrument observations on the morning of 14 August 2013. In Figure 10a, clear wave structures were observed on the east side of Shandong Peninsula (denoted by the red arrow) by the DNB at 01:58 LT. 10 crest rings can be seen. Their horizontal wavelength is measured to be about 20 km. Figure 10b shows the all-sky airglow imager network observation at 01:58 LT. Similar wave structures were observed by the all-sky airglow

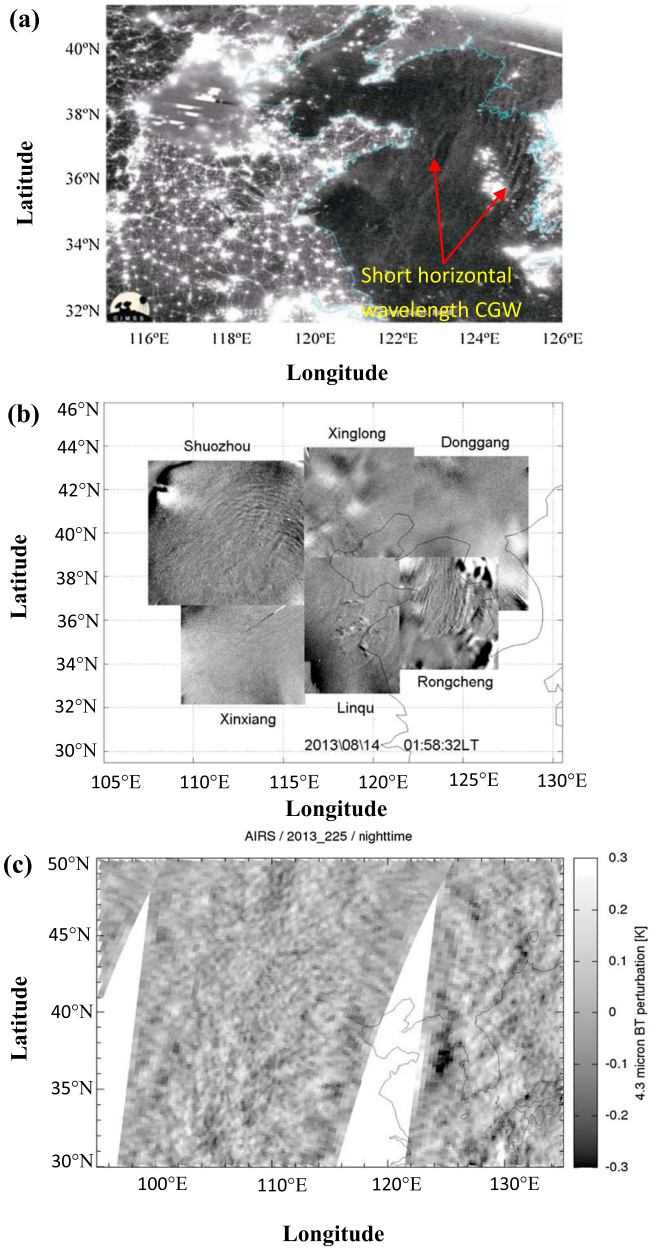

Figure 10. The multilayer observations of CGWs on 13–14 August 2013: (a) DNB observation at 01:58 LT, (b) all-sky airglow imager network observation at 01:58 LT, and (c) AIRS observations of stratospheric observation at 4.3 μm at 01:30 LT.

imager at the Rongcheng station, and the horizontal wavelength is also around 20 km, proving that satellites and the ground all-sky airglow imager observed the same CGWs. There are no other large-scale gravity waves in the OH airglow layer. Figure 10c presents AIRS observations of stratospheric CGWs at 4.3 μm at 01:30 LT. Also, there are no large-scale gravity waves in stratospheric region. Note that due to the coarser resolution of AIRS, it is not sensitive to GWs with short horizontal wavelengths.

In order to investigate the propagation characteristic of the CGW observed on 13 August 2013, the vertical wavelength of the CGW λ_z can be calculated from the gravity wave dispersion relation [*Isler et al.*, 1997]

$$m^2 = \frac{N^2}{(c-u)^2} + \frac{u_{zz}}{c-u} - k_h^2, \quad (5)$$

where $m = \frac{2\pi}{\lambda_z}$ and $k_h = \frac{2\pi}{\lambda_h}$ the vertical and horizontal wave number, respectively. The horizontal wavelength λ_h, and the horizontal phase speed c can be measured directly from the observations. u is the wind velocity the wave direction measured from meteor radar. u_{zz} is the second derivative of u with height z. N (Brunt-Väisälä frequency) is calculated from SABER temperature profile.

Equation (5) shows that the background wind velocity and temperature are very important for wave propagation analysis. The wind velocity in the mesopause region during this event was measured by the meteor radar at the Shisanling station (40.3°N, 116.2°E). The location of the meteor radar is marked by a yellow cross in Figure 1. The radar works at a frequency of 38.9 MHz, with a 7.5 kW transmit power. The radar measures wind velocities from 70 to 110 km with a time resolution of 1 h and a height interval of 2 km. Figure 11a presents the hodograph wind at 87 km for 20:00–04:00 LT obtained from the meteor radar on the night of 13 August 2013. The wind direction is almost southeastward from 20:00–03:00 LT. Figure 11b shows the wind in the southeastward propagating direction along the white dashed line in Figure 8 for 20:00–04:00 LT. The wind speed decreases from 58 m/s at 20:00 LT to 10 m/s at 04:00 LT.

During the CGW event, the TIMED (Thermosphere-Ionosphere-Mesosphere Energetics and Dynamics) satellite passed over Shandong Peninsula near (36.0°N, 119.1°E) at 02:31 LT. Figures 12a and 12b present temperature and OH 1.6 μm emission intensity measured by the SABER (Sounding of the Atmosphere using Broadband Emission Radiometry) instrument on board the TIMED satellite, respectively. A distinct

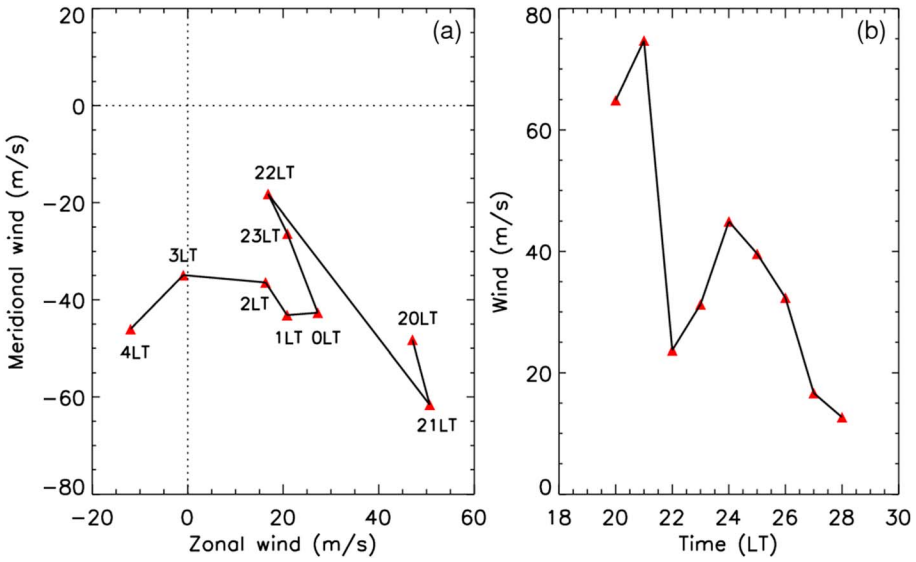

Figure 11. (a) Hodograph wind at 87 km for 20:00–04:00 LT obtained from meteor radar at the Shisanling station on the night of 13 August 2013. (b) Wind in the direction of the dashed line crossing the center of the CGW event is shown in Figure 8 for 20:00–04:00 LT.

temperature inversion layer, which is favorable for forming a thermal duct, can be observed from 85 to 93 km. The 1.6 μm OH emission profile reveals that the peak of the OH emission was at 89 km. The value of N^2 (square of Brunt-Väisälä frequency) is also shown in Figure 12a. Figure 12c gives the meteor radar wind profiles in propagating direction (southeastward) of CGW from 00:00 LT to 03:00 LT.

The vertical wave number m (Figure 12d) was calculated using the SABER temperature profile in Figure 12a and the meteor radar wind profile in Figure 12c by equation (5). From Figure 12d we can see that there is a ducting region from 83 km to 91 km in the mesopause region. This ducting layer in the mesopause region may explain why the measured horizontal wavelength values are the same (~20 km) from 400 km to 800 km radius. *Suzuki et al.* [2013b] also reported a ducted gravity wave propagating a long horizontal distance in the mesopause region from an airglow observation chain.

In order to investigate how the temperature and wind to affect the formation of the duct, the N^2 term (the first term on the right of equation (5)) and curvature term (the second term on the right of equation (5)) are shown in Figures 12e and 12f, respectively. We find the structure of the N^2 term is similar as the m^2 term. Also, the N^2 term is much larger than the curvature term. It suggests that the temperature plays a more dominant role than the wind in the formation of the duct.

The average horizontal wavelength is 21.6 ± 2.5 km from 00:00 LT to 03:00 LT, with the radius R ranging from 400 to 800 km. The horizontal phase speed is 59.7 ± 9.8 m/s. From equation (5), the average vertical wavelength is estimated to be around 9.6 ± 3.6 km, which is about the depth of the ducting layer (Figure 12d). For the freely propagating gravity wave, the zenith angle of the wave propagation (which can be estimated by $\mathrm{tg}^{-1}(\lambda_x/\lambda_z)$) is 66° [*Alexander and Holton*, 2004]. If a wave propagates freely from the tropopause (assumed to be 12 km) to OH layer (~87 km), then it should be observed at a radius of about 164 km. Therefore, the waves seen at the radius of 400–800 km cannot possibly be the waves that propagate from the tropopause region to the OH airglow layer directly.

The above analysis explains that the wave parameters are almost the same in the radius range of 400–800 km, as shown in Figure 9, most likely because these waves propagated horizontally inside a ducting layer.

3.3. Multiconvective Sources for the CGW Event on 9 August (#9-10)

Figure 13 displays the cloud maps in northern China observed by FY-2 from 21:00 to 03:00 LT. There were two isolated thunderstorm: one located at (33.8°N, 116.0°E) and another located at (35.4°N, 118.7°E) at 21:00 LT. After 21:00 LT, the storm in the southwest gradually moved northeast and became stronger. The other storm

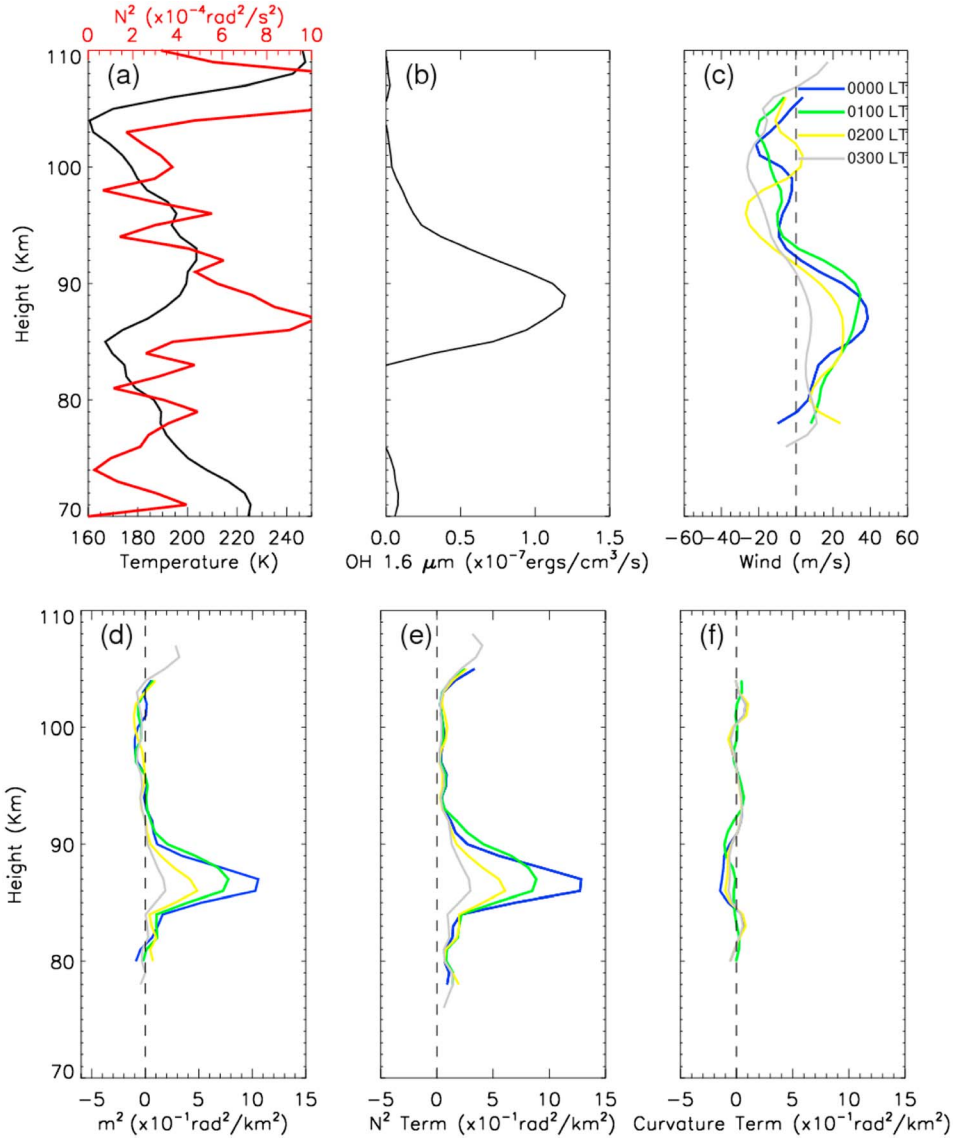

Figure 12. (a) Temperature and (b) OH 1.6 μm emission intensity obtained by the TIMED/SABER at 02:31 LT. (c) Meteor radar wind profile in propagating direction (southeastward) of CGW (east by south 15°) from 00:00 LT to 03:00 LT. (d) Vertical wave number m^2 derived from the temperature profile in Figure 12a and the meteor radar wind profiles in Figure 12c. The square of the Brunt-Väisälä frequency N^2 (red) derived from the temperature profile in Figure 12a. (e) N^2 term (the first term on the right of equation (5)) and (f) curvature term (the second term on the right of equation (5)).

(in the northeast) remained nearly stationary. After 01:00 LT, the two storms merged into one storm and lasted longer than 6 h. Two CGW events were observed by the network. Movie S2 shows the animated unwarped TD OH airglow images from 20:50 LT to 03:20 LT on 09–10 August 2013, illustrating the detailed evolution of the CGW event during the whole night.

From Movie S2 we can see that two CGWs can clearly be seen in the southeast of the Shuozhou station after 23:00 LT. Figure 13 shows that nearly 1 h prior to this event (at 22:00 LT), two isolated storms were located in the region of 34°N–36°N, 116°E–120°E.

The CGW event was also observed by VIIRS/Suomi NPP and AIRS/Aqua instruments. Figure 14 shows the multilayer observations of CGWs around 01:30 LT on 9 August 2013. Figure 14a displays the CGW event observed by VIIRS/Suomi NPP. Small-scale CGWs with a horizontal wavelength of ~20 km and large-scale CGW with a horizontal wavelength of ~100 km are observed by the DNB at 01:37 LT, indicated by red arrows in Figure 14a. Figure 14b shows the combined unwarped TD OH airglow image from six airglow imager

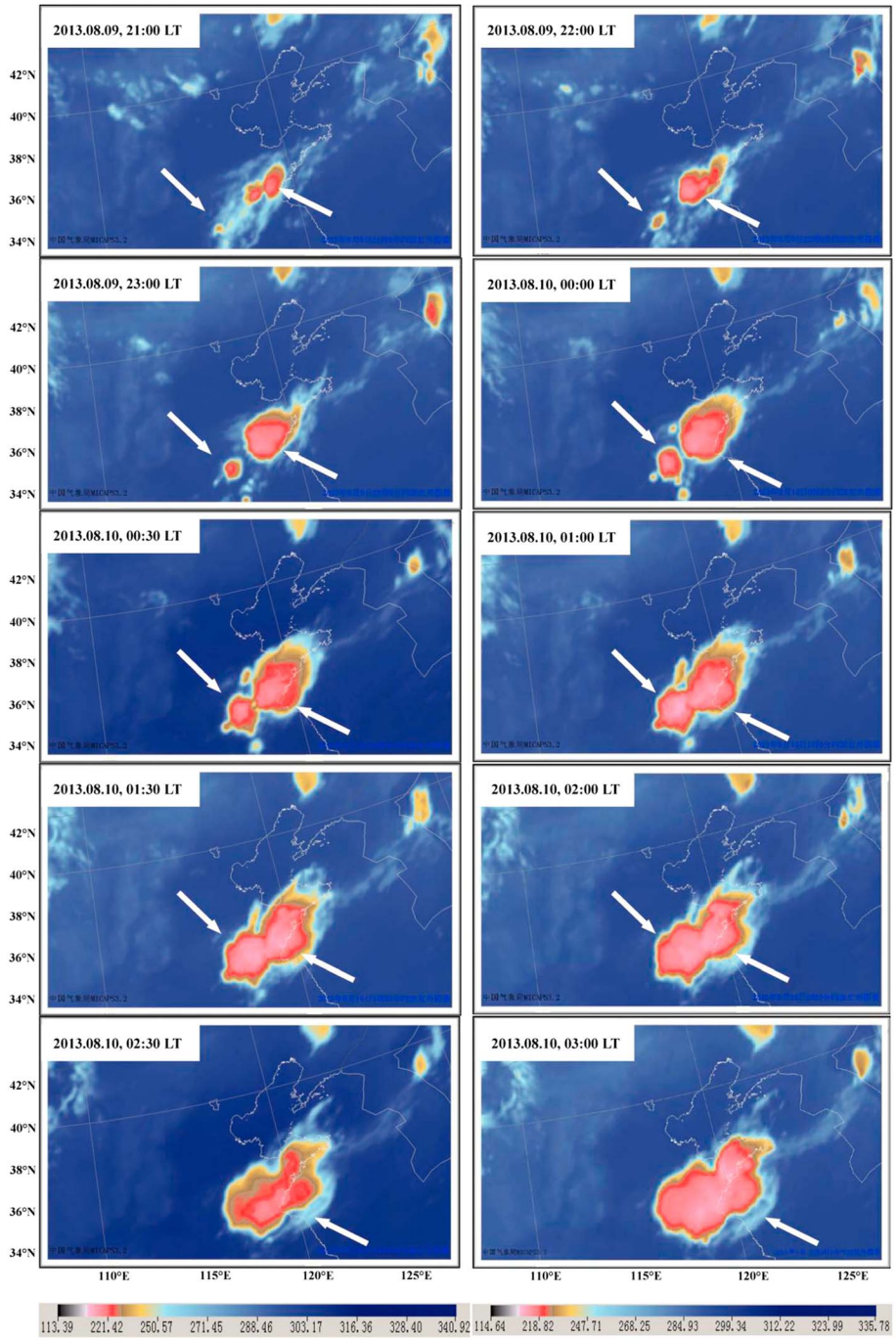

Figure 13. FY-2E (per hour) and FY-2D (per half hour) observations of cloud top brightness temperature from 21:00 LT to 03:00 LT on 9–10 August 2013.

observations at 01:41 LT. Clear circular wave structures can be seen at the Shouzhou, Xinglong, Xinxiang, and Rongcheng stations. Over the whole night, the thunderstorm took place near the Linqu and Donggang stations, so these stations were blocked by clouds and could not observe the wave event. However, the cloudy weather was favorable for VIIRS observation because the clouds blocked the city light and provided improved observation conditions of the OH airglow emission (see Figure 14a). Figure 14c presents the AIRS GW perturbations in brightness temperature at 01:30 LT on 9 August 2013. Stratospheric gravity waves were observed in the region of 34°N–36°N, 117°E–120°E with the horizontal wavelength of 100 km.

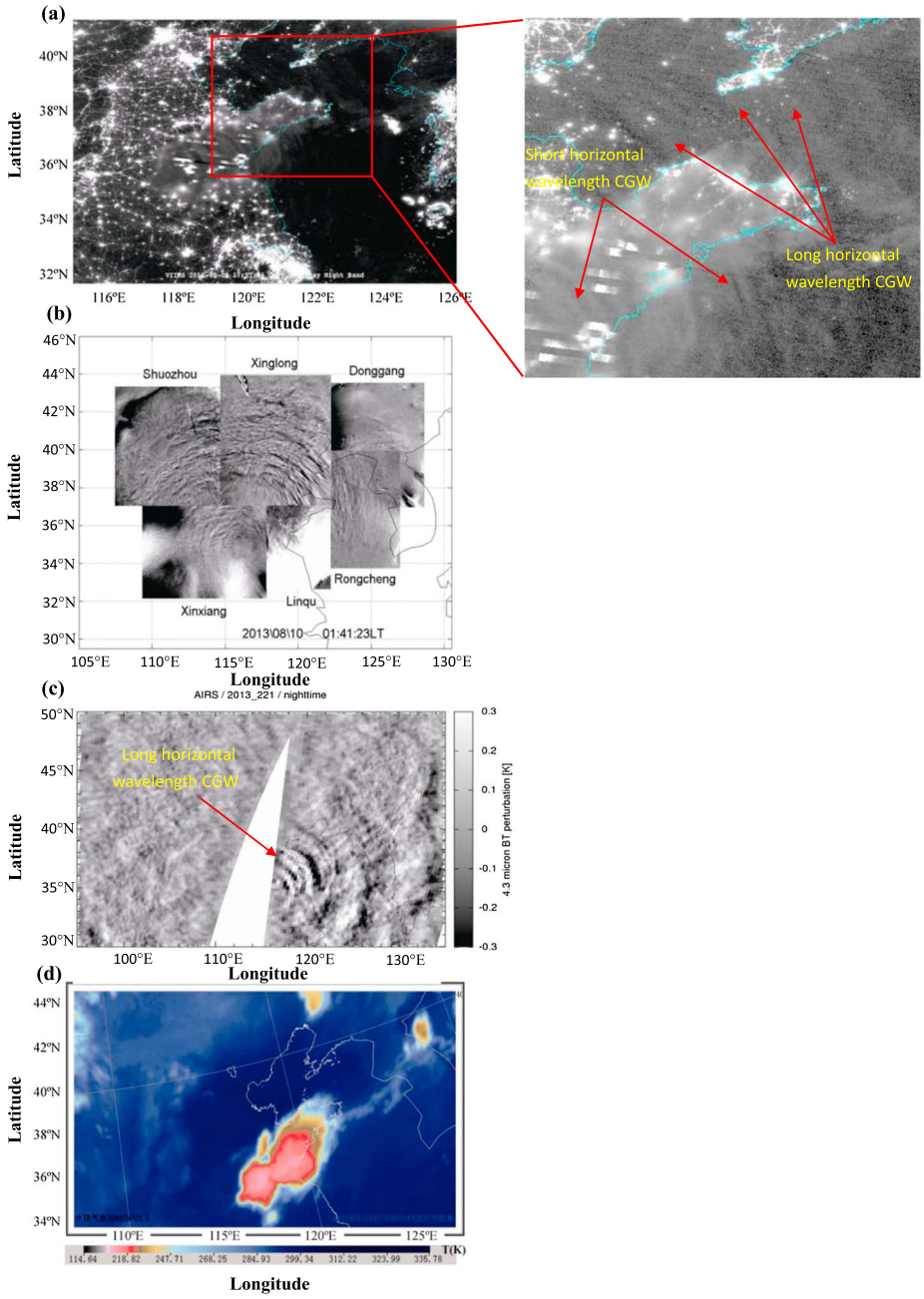

Figure 14. The multilayer observations of CGWs on 9 August 2013: (a) DNB observation at 01:30 LT, (b) all-sky airglow imager network observation at 01:41 LT, (c) AIRS observations of stratospheric observation at 4.3 μm at 01:30 LT, (d) FY-2 cloud observations at 01:00 LT.

Figure 14d gives the FY-2 cloud imagery at an earlier time (01:00 LT). The cloud was located in the region of 34°N–37°N, 116.5°E–121°E. Similarly, *Yue et al.* [2014] shows the two-layer observation of CGWs in the stratosphere and mesosphere using AIRS/Aqua and VIIRS/Suomi NPP observations, respectively.

Movie S2 shows that during this night, after 23:00 LT, there were no clouds over the Xinglong station. This can help elucidate the detailed evolution of the event. Other stations have occasional cloud contaminations. Here we mainly study the time evolution of the CGW event observed at the Xinglong station.

Figure 15 shows the two-level observations of CGWs on 9 August 2013. Figure 15a shows the combined unwarped TD OH airglow image from six all-sky airglow imager observations at 23:30 LT. Two CGWs

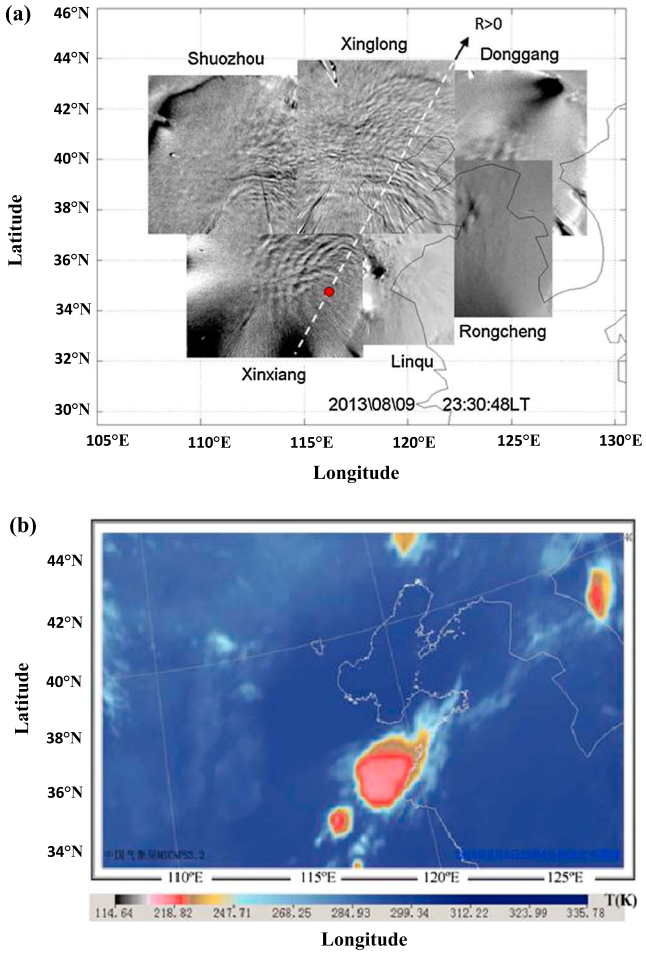

Figure 15. The two-layer observations of CGWs on 9 August 2013: (a) all-sky airglow imager network observation at 23:30 LT. The image along the dashed line crossing the midpoint (red dot) of two CGW events is used to study the gravity waves; (b) FY-2 cloud observations at 23:00 LT.

can be clearly seen southeast of the Shuozhou station. Figure 15b shows that about 30 min prior to this event, two isolated storms were located in the region of 34°N–36°N, 116°E–120°E.

We show the gravity waves along the line crossing through two centers of the CGW events from the observation at the Xinglong station, which is shown in Figure 15 (represented by the white dashed line), along with the time evolution in detail. Along this line, we can avoid the interference of the Milky Way. The origin of this line is located in the midpoint of the two centers of CGWs.

Figure 16 shows measured relative intensity perturbations ΔI/I (%) at the Xinglong station every 30 min from 23:00 LT to 03:30 LT along the dashed line in Figure 15. From the figure we can see that the multiple thunderstorms induced very large amplitude CGWs that occasionally reached 10% of the relative intensity perturbations (e.g., at 00:00 LT and 02:00 LT). Figure 6 indicates that the largest stroke count during the 3 years of observations occurred at DOY 221 (9 August) in this region and reached more than 14,000. Therefore, the strong perturbations of OH airglow are most likely induced by the multiple strong thunderstorms.

Figure 16 shows that the CGW on 9–10 August 2013 has very large horizontal wavelength about 200 km after 02:30 LT. At 01:30 LT the horizontal wavelength of the CGW observed at the Xinglong station was about 100 km, which is consistent with the observations from the satellites of VIIRS/Suomi NPP (see Figure 14a) and AIRS/Aqua (see Figure 14c) observations. The waves with the horizontal wavelength around 100 km frequently appeared throughout the whole night, lasting for more than 4.5 h from 23:00 LT to the end of the observation. These strong and persistent large-scale waves are most likely induced by these thunderstorms.

Figure 16 shows that aside from the waves with the wavelength of about 100 ~ 200 km, there were a lot of small-scale waves superposed on the larger-scale waves. For instance, at 00:30 LT and 01:00 LT, there are waves with wavelength of about 20 ~ 30 km.

It should be point out that there is background emission in the airglow measurement. For the background emission, with the aid of a simultaneous Fabry Perot interferometer measurement, *Swenson and Mende* [1994] suggested that the background contributed to ~30% of the total OH image signal. Through simultaneous OH airglow intensity observed by Spectral Airglow Temperature Imager, *Suzuki et al.* [2007b] also found that the background emission accounted for ~30% of the total OH image signal. Because of the lack of equipment to quantify the background emission, we cannot accurately estimate the background emission contribution to the total image signal. Additionally, the background emission varies with the atmospheric conditions. Therefore, the background is not considered in this work. So, d*I*/*I* is probably underestimated.

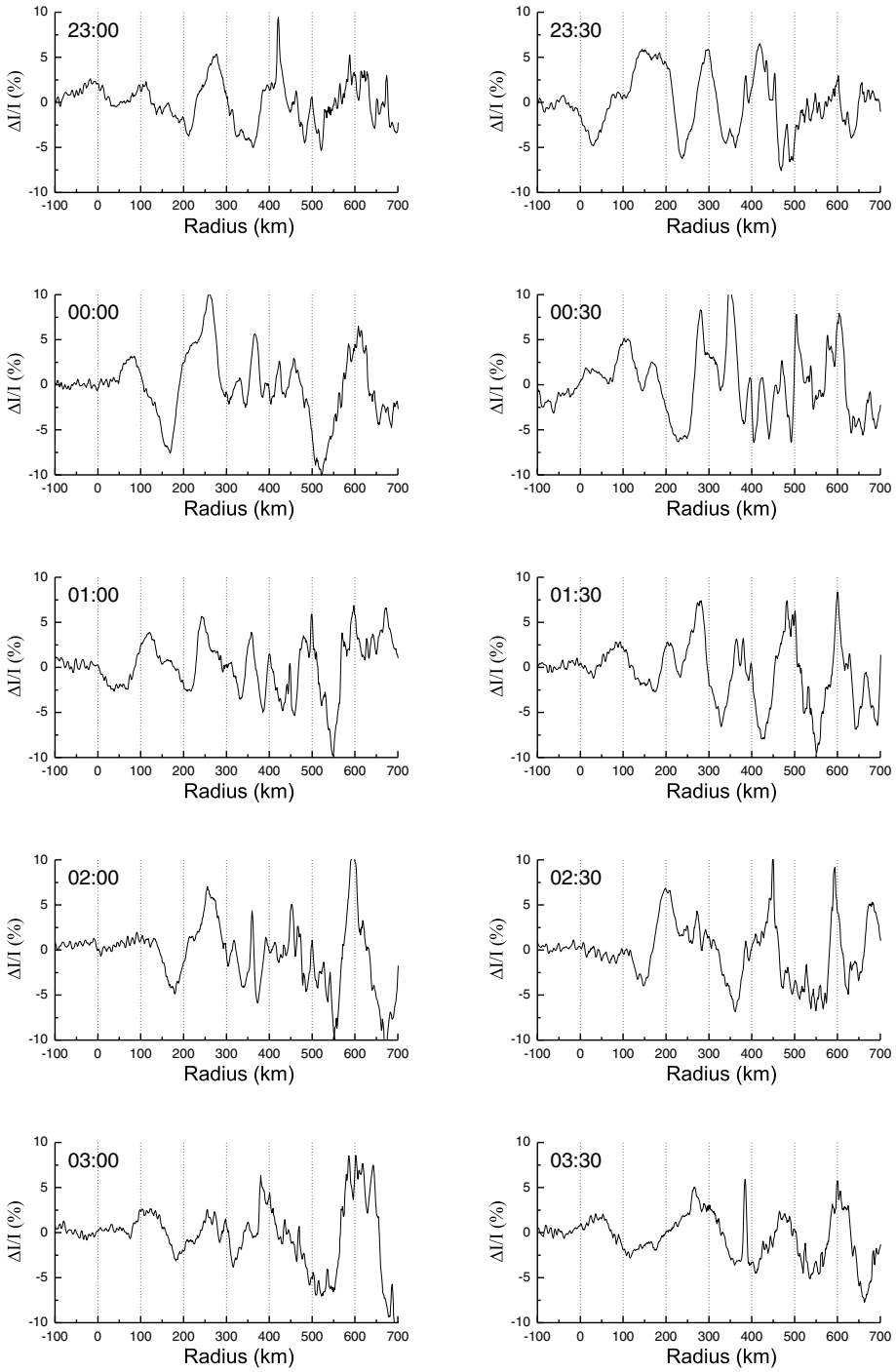

Figure 16. Measured relative intensity perturbations $\Delta I/I$ (%) at every half hour from 23:00 LT to 03:30 LT on 9 August 2013 as a function of radius from the midpoint of two apparent centers of the concentric rings in the direction to the northeast, which is shown as a dashed line in Figure 15a.

4. Summary

The first no-gap OH airglow all-sky imager network in the world was established in northern China in February 2012. The network is composed of six all-sky airglow imagers. This network can make observations of gravity waves at the OH airglow layer in an area roughly 2000 km east and west and about 1400 km north and south. The network can provide the detailed information about the gravity wave temporal evolution in a

wider range compared to a single airglow imager. The wide observation range facilitates the comparison with satellite observations, which is in favor of studying the propagation and evolution of GWs at multilayers.

Using this no-gap OH airglow imager network, we observed a large number of CGW events on 13 nights in first half of August 2013. These intensive CGW events were rare and unusual during the 3 years of the network observations compared with previous ground observations.

We compare thunderstorm activities using the CAPE from ECMWF reanalysis and the lightning stroke rate from WWLLN between 2012, 2013, and 2014. The results show that summer 2013 was special with more frequent thunderstorms occurring in north China, especially in the first half of August, than in 2012 and 2014. The all-sky imager network also observed more CGW events in summer 2013 than in the summers of 2012 and 2014.

In this work, we combine the network data with satellite observations to investigate the propagation and evolution of these CGWs in the stratosphere and mesopause. The geostationary FY-2 satellites provide the temporal evolution of the thunderstorm systems. The AIRS/Aqua displays the CGWs in the stratosphere. VIIRS/Suomi NPP shows the CGWs in the OH airglow layer.

From these joint observations, we investigate the temporal and spatial evolution of two representative long-lasting CGW events in detail. The first of which is induced by only one strong convective source on the night of 13 August (#13-14). The other that was caused by multiple storm sources is on the night of 9 August (#9-10). These two strong CGW events lasted several hours and followed the temporal evolutions of thunderstorms very well.

For the CGW event on 13 August 2013(#13-14), we find that within less than 300 km from the CGW center, the measured horizontal wavelengths agree with the GW dispersion relation. It is interesting that likely due to the ducting effect, the CGW propagated a long distance horizontally in the mesopause, which is also confirmed by VIIRS/Suomi NPP.

For the CGW event on 9 August 2013(#9-10), multiscale wave structures from less than 10 km to 200 km and with large perturbations of 10% were observed. These waves were probably induced by the superposition of strong multiple thunderstorms. The large-scale CGWs (~100 km horizontal wavelength) were simultaneously observed in the mesopause by the airglow imager network and VIIRS/Suomi NPP, as well as in the stratosphere by AIRS/Aqua.

The two events (#13-14 and #9-10) combined with satellite observations from FY-2, AIRS/Aqua, and VIIRS/Suomi NPP, provide multilevel observations of the CGWs from the stratosphere to the mesopause region. These observations give strong evidence of the coupling between the lower atmosphere weather and upper atmosphere dynamics. We will investigate the coupling of wave energy between different layers in detail in future work.

Acknowledgments

We would like to thank Han-Li Liu's suggestions and comments on this work. FY-2 cloud data and MICAPS used in this study are provided by Dalian Meteorological Observatory, Dalian, China, and China Meteorological Administration. AIRS data are distributed by the NASA Goddard Earth Sciences Data Information and Services Center (GES DISC). The VIIRS Sensor Data Record data are distributed by the CIMSS Atmospheric Product and Evaluation and Test Elements (PEATE) and NOAA Comprehensive Large Array-data Stewardship System (CLASS). We thank the TIMED/SABER team for providing the data used in this paper. We also thank the ECMWF for providing the CAPE data and the WWLLN team for providing the lightning stroke count data. This work was supported by the National Science Foundation of China (41331069 and 41229001) and the Chinese Academy of Sciences (KZZD-EW-01-2). The project is also supported by the Specialized Research Fund for State Key Laboratories. We acknowledge the use of data from the Chinese Meridian Project. The imager network data are archived and can be provided upon the request to the corresponding author (xujy@nssc.ac.cn).

References

Alexander, M. J., and J. R. Holton (2004), On the spectrum of vertically propagating gravity waves generated by a transient heat source, *Atmos. Chem. Phys.*, *4*, 923–932.

Alexander, M. J., P. T. May, and J. H. Beres (2004), Gravity waves generated by convection in Darwin area during the Darwin Area Wave Experiment, *J. Geophys. Res.*, *109*, D20S04, doi:10.1029/2004JD004729.

Aumann, H. H., et al. (2003), AIRS/AMSU/HSB on the aqua mission: Design, science objectives, data products, and processing systems, *IEEE Trans. Geosci. Remote Sens.*, *41*, 253–264.

Aumann, H. H., D. Gregorich, and S. M. DeSouza-Machado (2006), AIRS observations of deep convective clouds, *Proc. SPIE 6301*, 63010J, doi:10.1117/12.681201.

Bluestein, H. B., E. W. McCaul Jr., G. P. Byrd, and G. R. Woodall (1988), Mobile sounding observations of a tornadic storm near the dryline: The Canadian, Texas storm of 7 May 1986, *Mon. Weather Rev.*, *116*, 1790–1804.

Chamberlain, J. W. (1961), *Physics of the Aurora and Airglow*, Academic Press, New York.

Cummins, K. L., and M. J. Murphy (2009), An overview of lightning locating systems: History, techniques, and data uses, with an in-depth look at the U. S. NLDN, *IEEE Trans. Electromagn. Compat.*, *51*(3), 499–518.

Dee, D. P., et al. (2011), The ERA-Interim reanalysis: Configuration and performance of the data assimilation system, *Q. J. R. Meteorol. Soc.*, *137*, 553–597.

Fritts, D. C., and M. J. Alexander (2003), Gravity wave dynamics and effects in the middle atmosphere, *Rev. Geophys.*, *41*(1), 1003, doi:10.1029/2001RG000106.

Garcia, F. J., M. J. Taylor, and M. C. Kelley (1997), Two-dimensional spectral analysis of mesospheric airglow image data, *Appl. Opt.*, *36*(29), 7374–7385, doi:10.1364/AO.36.007374.

Gong, J., D. L. Wu, and S. D. Eckermann (2012), Gravity wave variances and propagation derived from AIRS radiances, *Atmos. Chem. Phys.*, *12*(4), 1701–1720.

Gong, J., J. Yue, and D. L. Wu (2015), Global survey of concentric gravity waves in AIRS images and ECMWF analysis, *J. Geophys. Res. Atmos.*, *120*, 2210–2228, doi:10.1002/2014JD022527.

Hoffmann, L., and M. J. Alexander (2010), Occurrence frequency of convective gravity waves during the North American thunderstorm season, *J. Geophys. Res.*, *115*, D20111, doi:10.1029/2010JD014401.

Hoffmann, L., X. Xue, and M. J. Alexander (2013), A global view of stratospheric gravity wave hotspots located with Atmospheric Infrared Sounder observations, *J. Geophys. Res. Atmos.*, *118*, 416–434, doi:10.1029/2012JD018658.

Horinouchi, T., T. Nakamura, and J.-I. Kosaka (2002), Convectively generated mesoscale gravity waves simulated throughout the middle atmosphere, *Geophys. Res. Lett.*, *29*(21), 2007, doi:10.1029/2002GL016069.

Hutchins, M. L., R. H. Holzworth, J. B. Brundell, and C. J. Rodger (2012), Relative detection efficiency of the World Wide Lightning Location Network, *Radio Sci.*, *47*, RS6005, doi:10.1029/2012RS005049.

Isler, J. R., M. J. Taylor, and D. C. Fritts (1997), Observational evidence of wave ducting and evanescence in the mesosphere, *J. Geophys. Res.*, *102*(D22), 26,301–26,313, doi:10.1029/97JD01783.

Kubota, M., H. Fukunishi, and S. Okano (2001), Characteristics of medium- and large-scale TIDs over Japan derived from OI 630-nm nightglow observation, *Earth Planets Space*, *53*, 741–751.

Lane, T. P., R. D. Sharman, T. L. Clark, and H.-M. Hsu (2003), An investigation of turbulence generation mechanisms above deep convection, *J. Atmos. Sci.*, *60*, 1297–1321, doi:10.1175/1520-0469(2003)60<1297:AIOTGM>2.0.CO;2.

Li, Q., J. Xu, J. Yue, W. Yuan, and X. Liu (2011), Statistical characteristics of gravity wave activities observed by an OH airglow imager at Xinglong, in northern China, *Ann. Geophys.*, *29*, 1401–1410, doi:10.5194/angeo-29-1401-2011.

Li, Q., J. Xu, J. Yue, X. Liu, W. Yuan, B. Ning, S. Guan, and J. P. Younger (2013), Investigation of a mesospheric bore event over northern China, *Ann. Geophys.*, *31*, 409–418.

Liu, A. Z., and G. R. Swenson (2003), A modeling study of O_2 and OH airglow perturbations induced by atmospheric gravity waves, *J. Geophys. Res.*, *108*(D4), 4151, doi:10.1029/2002JD002474.

Miller, S. D., S. P. Mills, C. D. Elvidge, D. T. Lindsey, T. F. Lee, and J. D. Hawkins (2012), Suomi satellite brings to light a unique frontier of nighttime environmental sensing capabilities, *Proc. Natl. Acad. Sci. U.S.A.*, *109*(39), 15,706–15,711, doi:10.1073/pnas.1207034109.

Piani, C., D. Durran, M. J. Alexander, and J. R. Holton (2000), A numerical study of three-dimensional gravity waves triggered by deep tropical convection and their role in the dynamics of the QBO, *J. Atmos. Sci.*, *57*(22), 3689–3702, doi:10.1175/1520-0469(2000)057<3689:ANSOTD>2.0.CO;2.

Rienecker, M. M., et al. (2011), MERRA: NASA's Modern-ERA Retrospective Analysis for Research and Applications, *J. Clim.*, *24*, 3624–3648.

Rodger, C. J., J. B. Brundell, and R. L. Dowden (2005), Location accuracy of VLF World Wide Lightning Location (WWLL) network: Post-algorithm upgrade, *Ann. Geophys.*, *23*, 277–290.

Rodger, C. J., S. W. Werner, J. B. Brundell, N. R. Thomson, E. H. Lay, R. H. Holzworth, and R. L. Dowden (2006), Detection efficiency of the VLF World-Wide Lightning Location Network (WWLLN): Initial case study, *Ann. Geophys.*, *24*, 3197–3214.

Sentman, D. D., E. M. Wescott, R. H. Picard, J. R. Winick, H. C. Stenbaek-Nielsen, E. M. Dewan, D. R. Moudry, F. T. Sao Sabbas, M. J. Heavner, and J. Morrill (2003), Simultaneous observations of mesospheric gravity waves and sprites generated by a midwestern thunderstorm, *J. Atmos. Sol. Terr. Phys.*, *65*, 537–550, doi:10.1016/S1364-6826(02)00328-0.

Suzuki, S., K. Shiokawa, Y. Otsuka, T. Ogawa, K. Nakamura, and T. Nakamura (2007a), A concentric gravity wave structure in the mesospheric airglow images, *J. Geophys. Res.*, *112*, D02102, doi:10.1029/2005JD006558.

Suzuki, S., K. Shiokawa, Y. Otsuka, T. Ogawa, M. Kubota, M. Tsutsumi, T. Nakamura, and D. C. Fritts (2007b), Gravity wave momentum flux in the upper mesosphere derived from OH airglow imaging measurements, *Earth Planets Space*, *59*, 421–428.

Suzuki, S., S. L. Vadas, K. Shiokawa, Y. Otsuka, S. Kawamura, and Y. Murayama (2013a), Typhoon-induced concentric airglow structures in the mesopause region, *Geophys. Res. Lett.*, *40*, 5983–5987, doi:10.1002/2013GL058087.

Suzuki, S., K. Shiokawa, Y. Otsuka, S. Kawamura, and Y. Murayama (2013b), Evidence of gravity wave ducting in the mesopause region from airglow network observations, *Geophys. Res. Lett.*, *40*, 601–605, doi:10.1029/2012GL054605.

Swenson, G., and S. B. Mende (1994), OH emission and gravity waves (including a breaking wave) in all-sky imagery from Bear Lake, UT, *Geophys. Res. Lett.*, *21*, 2239–2242, doi:10.1029/94GL02112.

Taylor, M. J., and M. A. Hapgood (1988), Identification of a thunderstorm as a source of short period gravity waves in the upper atmospheric nightglow emissions, *Planet. Space Sci.*, *36*, 975–985.

Vadas, S. L., J. Yue, C.-Y. She, P. Stamus, and A. Z. Liu (2009), A model study of the effects of winds on concentric rings of gravity waves from a convective plume near Fort Collins on 11 May 2004, *J. Geophys. Res.*, *114*, D06103, doi:10.1029/2008JD010753.

Vadas, S., J. Yue, and T. Nakamura (2012), Mesospheric concentric gravity waves generated by multiple convective storms over the North American Great Plain, *J. Geophys. Res.*, *117*, D07113, doi:10.1029/2011JD017025.

Wang, C. (2010), New chains of space weather monitoring stations in China, *Space Weather*, *8*, S08001, doi:10.1029/2010SW000603.

Williams, E., K. Rothkin, D. Stevenson, and D. Boccippio (2000), Global lightning variations caused by changes in thunderstorm flash rate and by changes in the number of thunderstorms, *J. Appl. Meteorol.*, *39*, 2223–2230.

Yue, J., S. L. Vadas, C.-Y. She, T. Nakamura, S. C. Reising, H.-L. Liu, P. Stamus, D. A. Krueger, W. Lyons, and T. Li (2009), Concentric gravity waves in the mesosphere generated by deep convective plumes in the lower atmosphere near Fort Collins, Colorado, *J. Geophys. Res.*, *114*, D06104, doi:10.1029/2008JD011244.

Yue, J., L. Hoffmann, and M. Joan Alexander (2013), Simultaneous observations of convective gravity waves from a ground-based airglow imager and the AIRS satellite experiment, *J. Geophys. Res. Atmos.*, *118*, 3178–3191, doi:10.1002/jgrd.50341.

Yue, J., S. Miller, L. Hoffmann, and W. Straka III (2014), Stratospheric and mesospheric gravity waves over Tropical Cyclone Mahasen: Joint AIRS and VIIRS satellite observations, *J. Atmos. Sol. Terr. Phys.*, *119*, 83–90, doi:10.1016/j.jastp.2014.07.003.